HHS Public Access

Author manuscript

Eur J Nucl Med Mol Imaging. Author manuscript; available in PMC 2018 June 01.

Published in final edited form as:

Eur J Nucl Med Mol Imaging. 2018 June ; 45(6): 989–998. doi:10.1007/s00259-018-3939-x.

Combined model-based and patient-specific dosimetry for ^{18}F-DCFPyL, a PSMA-targeted PET agent

Donika Plyku[1], **Esther Mena**[1], **Steven P. Rowe**[1], **Martin A. Lodge**[1], **Zsolt Szabo**[1], **Steve Y. Cho**[1,2], **Martin G. Pomper**[1,3], **George Sgouros**[1,4], and **Robert F. Hobbs**[1,4]

[1]The Russell H. Morgan Department of Radiology and Radiological Science, School of Medicine, Johns Hopkins University, Baltimore, MD, USA

[2]Department of Radiology, School of Medicine and Public Health, University of Wisconsin, CRB II 4M.60, 1550 Orleans St., Baltimore, MD 21287, USA

[3]Sidney Kimmel Comprehensive Cancer Center, Johns Hopkins Medical Institutions, Baltimore, MD, USA

[4]Department of Radiation Oncology, School of Medicine, Johns Hopkins University, CRB II 4M.60, 1550 Orleans St., Baltimore, MD, USA

Abstract

Purpose—Prostate-specific membrane antigen (PSMA), a type-II integral membrane protein highly expressed in prostate cancer, has been extensively used as a target for imaging and therapy. Among the available PET radiotracers, the low molecular weight agents that bind to PSMA are proving particularly effective. We present the dosimetry results for ^{18}F-DCFPyL in nine patients with metastatic prostate cancer.

Methods—Nine patients were imaged using sequential PET/CT scans at approximately 1, 12, 35 and 70 min, and a final PET/CT scan at approximately 120 min after intravenous administration of 321 ± 8 MBq (8.7 ± 0.2 mCi) of^{18}F-DCFPyL. Time-integrated-activity coefficients were calculated and used as input in OLINDA/EXM software to obtain dose estimates for the majority of the major organs. The absorbed doses (AD) to the eye lens and lacrimal glands were calculated using Monte-Carlo models based on idealized anatomy combined with patient-specific volumes and activity from the PET/CT scans. Monte-Carlo based models were also developed for calculation of the dose to two major salivary glands (parotid and submandibular) using CT-based patient-specific gland volumes.

Results—The highest calculated mean AD per unit administered activity of ^{18}F was found in the lacrimal glands, followed by the submandibular glands, kidneys, urinary bladder wall, and parotid glands. The *S*-values for the lacrimal glands to the eye lens (0.42 mGy/MBq h), the tear film to the eye lens (1.78 mGy/MBq h) and the lacrimal gland self-dose (574.10 mGy/MBq h) were calculated. Average *S*-values for the salivary glands were 3.58 mGy/MBq h for the parotid self-dose and 6.78 mGy/MBq h for the submandibular self-dose. The resultant mean effective dose of ^{18}F-DCFPyL was 0.017 ± 0.002 mSv/MBq.

Correspondence to: Robert F. Hobbs.

Conclusions—^{18}F-DCFPyL dosimetry in nine patients was obtained using novel models for the lacrimal and salivary glands, two organs with potentially dose-limiting uptake for therapy and diagnosis which lacked pre-existing models.

Keywords

PSMA; PET; Prostate cancer; ^{18}F; Dosimetry; Monte-Carlo modeling

Introduction

Prostate cancer (PCa) is the most common type of cancer among men in the USA and the second most common cause of cancer-related death in men, with an estimated 180,890 new cases annually [1]. In Europe, PCa is the second most common cancer in men and the fourth most common malignancy overall, with an estimated 90,000 deaths annually [2]. Castration-resistant PCa is defined by progression occurring in the presence of castrate-level testosterone values. Progression can be biochemical, that is a rise in prostate-specific antigen levels, or clinical/radiographic, that is appearance of metastases [3]. Sensitivity and specificity limitations of conventional imaging modalities, including contrast-enhanced computed tomography (CT), ^{99m}Tc-MDP (methylene diphosphonate) bone scan, ultrasonography and magnetic resonance imaging (MRI), have triggered the need to develop new functional imaging tools in this field.

Positron emission tomography (PET) using 2-deoxy-2-[^{18}F]fluoro-D-glucose (FDG PET) is a major clinical tool in cancer diagnosis. FDG is suitable for the detection of many types of cancer, but its utility for imaging PCa is unclear [4–6]. Recently, PET radiotracers that bind to PSMA have been extensively studied [7–12]. As a functional imaging modality, PET provides improved spatial resolution, easier and more accurate quantitation, and a higher sensitivity compared with single photon emission tomography [7, 13]. Further, PSMA is an outstanding target for imaging PCa due to near-universal expression on PCa tumors and a positive correlation between expression levels and disease aggressiveness. For these reasons, PSMA-targeted imaging agents that are labeled with PET radionuclides may achieve high accuracy in disease detection.

PSMA, known as folate hydrolase I or glutamate carboxy-peptidase II, is a 750-amino acid type-II transmembrane glycoprotein primarily expressed in normal human prostate epithelium. PSMA is expressed at lower levels by cells in the small intestine, proximal renal tubules and salivary glands (SG). PSMA is highly expressed in poorly differentiated, metastatic and hormone-refractory carcinomas, such as in castration-resistant metastatic PCa. For these reasons, PSMA is an excellent target for imaging and targeted systemic treatment of PCa.

Various PET radiotracers have been introduced for imaging PCa [8–12, 14, 15]. The low molecular weight (LMW) agents have several advantages in terms of PSMA binding, relative to large molecules, such as higher ability to enter solid tumors and faster blood clearance [16]. ^{18}F-DCFBC (*N*-[*N*-[(*S*)-1,3-dicarboxypropyl]carbamoyl]-4-^{18}F-fluorobenzyl-L-cysteine) and ^{18}F-DCFPyL (2-(3-(1-carboxy-5-[(6-[^{18}F]fluoro-pyridine-3-carbonyl)-amino]-pentyl)-ureido)-pentanedioic acid) are two PSMA-targeted LMW PET

imaging agents radiolabeled with ^{18}F-fluoride that have shown high affinity for PSMA [17]. Cho et al. described the synthesis of and the first human imaging experience with the first-generation LMW inhibitor of PSMA, ^{18}F-DCFBC [18]. Recently, Szabo et al. reported on the second-generation LMW PSMA-targeted radiotracer ^{18}F-DCFPyL [19], which was developed in part to address a potential limitation of ^{18}F-DCFBC related to the observed blood pool activity that could interfere with the detection of lymph-node metastases in the retroperitoneum and pelvis that are adjacent to large blood vessels. Preclinical studies with^{18}F-DCFPyL demonstrated a higher binding affinity for PSMA and a first-in-human study showed a lower activity within the blood pool [19]. The advantages of using ^{18}F-DCFPyL over other PET radiopharmaceutical agents available for the imaging of PCa, such as^{11}C/^{18}F-choline, ^{18}F-FACBC, ^{68}Ga-PSMA, ^{18}F-bombesin, and ^{64}Cu/^{68}Ga/^{18}F-uPAR, are the ability to differentiate between indolent and aggressive disease in the prostate gland and the ability to be distributed by industry [20]. The weaknesses associated with ^{18}F-DCFPyL are increased blood vessel pool activity, although better than ^{18}F-DCFBC, and limited clinical evidence to date [20].

The radiation dosimetry results in the first four patients and preliminary dose estimates for the eye lens (EL), lacrimal glands (LG) and SG were included in the report of the first-in-human study of ^{18}F-DCFPyL [19]. Surrogate *S*-values were used for the preliminary dose estimates to target organs for which no *S*-values are currently available (EL, LG and SG), however, high uptake visible in the LG and SG necessitated a more in-depth dosimetric analysis.

Here we report the dose results for the whole patient dataset in the study, which now includes Monte-Carlo model-based and patient-specific dosimetry results for the EL, LG and SG. The dose calculations for these organs cannot be performed with presently available, standard organ dosimetry software packages such as OLINDA/EXM [21]. We introduce newly developed, previously unavailable Monte-Carlo models for calculation of the doses to these nonstandard target organs for ^{18}F.

Materials and methods

Chemistry

Radiochemistry related to the preparation of ^{18}F-DCFPyL (Fig. 1) has been previously reported [17, 19]. An average radiochemical yield of 2.8 ± 1.2%, with a specific activity of 159 ± 45 GBq/μmol and 100% radiochemical purity (n = 9), was achieved.

Patients and study design

The study was approved by the Institutional Review Board at Johns Hopkins University. Written consent was obtained from nine patients recruited from the Johns Hopkins Prostate Cancer/Genitourinary Oncology Program. Food and Drug Administration approval was obtained under an exploratory investigational new drug application (eIND #121,064). Included patients had both histological evidence of PCa and radiological evidence of new and progressive metastatic disease and prostate-specific antigen blood levels of 1 ng/ml or

higher [19]. Approximately 320.6 MBq (range 310.8–327.1 MBq; 8.66 mCi, range 8.40–8.84 mCi) ^{18}F-DCFPyL was injected intravenously.

PET imaging

Patients were imaged via sequential PET/CT scans using a Discovery DRX PET/CT scanner (GE Healthcare, Waukesha, WI) in three-dimensional (3D) acquisition mode. Each patient was injected with activity, then an initial low-dose CT scan was acquired immediately for attenuation correction and volume of interest (VOI) definition. Subsequently, four PET scans from the mid-thigh to the skull vertex were acquired sequentially starting at approximately 1, 12, 35, and 70 min after injection. The first scan was acquired using 1 min/bed position, the second using 2 min/bed position, and the third and fourth used 4 min/bed position. After the patient had voided, a second low-dose CT scan and a final PET scan, using 4 min/bed position, were acquired starting at approximately 120 min after injection.

Radiation dosimetry

Dosimetry calculations were performed according to the Medical Internal Radiation Dose (MIRD) *S*-value methodology [22]. Contours of organs of interest were drawn on both CT scans using the MIM software package (MIM Software, Cleveland, OH). Organs included: adrenal glands, urinary bladder, bone marrow, brain, gallbladder, heart, heart wall, kidneys, LG, EL, liver, small intestine, lower large intestine, upper large intestine, lungs, muscle, pancreas, parotid glands (PG), spleen, stomach, submandibular glands (SMG), testes, thyroid and whole body. The kidneys as well as the small organs in the head and neck bed that demonstrated uptake such as the LG, PG and SMG were also drawn on each PET scan. The activity at each time-point for these organs was extracted from the PET images, while the “true” volume was determined from VOIs drawn on the CT scans (average of two CT scans). The largest difference in organ volumes between the two CT scans was 50%.

To account for partial volume effects, two different methods were applied according to the size of the organ volumes: one a traditional recovery coefficient method for the SG and a different method for the LG. The final activity in the LG was determined by subtraction of background activity following the small volume activity measurement methodology proposed by Plyku et al. [23]. For the recovery coefficient method, a NEMA phantom containing six spheres with diameters 10, 13, 17, 22, 28 and 37 mm was filled with ^{18}F and water with a sphere-to-background activity ratio of 4:1 and imaged using a GE Discovery DRX PET/CT scanner, following which resolution recovery coefficients for ^{18}F were calculated. A correction was applied to the measured time–activity data of the PG and SMG assuming a spherical shape with a reference volume calculated using reference masses and reference density values from ICRP 89 [24]. The corrected activity values were 17% and 21% higher than the measured activity values for the PG and SMG, respectively. The whole-body activity was considered to be equal to the total activity in the available field of view (mid-thigh to skull vertex), assuming that the activity in the parts of the body outside the field of view is negligible.

In the few cases in which the entire organ volume could not be separated from the adjacent structures or in which the whole organ could not be drawn (e.g., heart wall, bone marrow

and muscle), a partial VOI was drawn to estimate the organ activity concentration. The organ activity was then calculated by multiplying the activity concentration by the VOI volume drawn on the CT scan, plotted as a function of time and fit to calculate the time-integrated activity (TIA). The calculated TIA was then scaled to the reference adult male total organ mass.

The time–activity curves were fitted to monoexponential or double-exponential functions, when reasonable, or a hybrid (trapezoidal + monoexponential function to the last two or three data points) fit, and then integrated to obtain the TIA or activity concentration. Fitting was performed using SAAM II (The Epsilon Group, Charlottesville, VA) [25]. TIA coefficients (TIACs) were obtained by dividing the TIA by the injected activity. Whole-organ TIACs were divided by the patient-specific organ masses obtained using CT VOIs and reference organ densities [24, 26] to obtain TIAC concentrations. Patient organ masses available from the CT scans were compared with organ masses in OLINDA/EXM [21], and for those organs for which a large difference (>20%) was calculated, organ masses in OLINDA/EXM were adjusted to match the patient organ masses. This compromise was made to be consistent with the methodology used in the previous study [19]. The TIAC concentrations were multiplied by either the reference organ masses listed in OLINDA/EXM or the adjusted organ masses (organs for which the mass was adjusted as described previously) to give scaled organ TIACs. The resulting TIACs were used as input to OLINDA/EXM to obtain absorbed doses (AD). The weighting factors used in the effective dose calculation were based on recommendations in ICRP 60 [27], as implemented in OLINDA/EXM. The MIRD bladder model with a voiding interval of 1.5 h, the biological whole-body clearance half-life and a voiding fraction of 1 was used to calculate bladder AD [28].

Dosimetry calculations for the lens of the eye, and the lacrimal and salivary glands

Separate calculations were performed to calculate the ADs for the EL, LG, PG and SMG. GEANT4 Monte Carlo simulations were used to obtain the *S*-values *S*(EL ←LG) and *S*(LG ←LG). GEANT4 is a high-energy physics toolkit used to simulate radiation transport [29]. Simple geometric shapes were used to represent the eyeball, EL and LG. Front and side views of the model are shown in Fig. 2. A sphere with radius 12 mm [26] is used to represent each eyeball and an ellipsoid with axes of 9 mm in width in two dimensions and an axial thickness 4 mm was used for each lens [24]. The center of the lens is positioned 9 mm away anteriorly from the center of each respective eyeball. An ellipsoid was used to represent each LG; these had axial ratios of 5:5:14.6 based on measurements performed by Tamboli et al. on CT images [30] and with patient-specific total volumes based on CT VOI contours. The center of the LG ellipse was positioned 6 mm away laterally (Fig. 2) and 15 mm superiorly in relation to the center of the eyeball. These distances as well as the distance between the two eyeballs were determined by taking an average value from the patients' CT images.

The dose contribution from the LG to the EL is the product of the *S*-value (EL ← LG) and the TIA of the LG, from both LGs. The TIA was determined by integrating the fitted time–activity curves for each patient plotted using the time–activity data from each VOI. The

activity value for each time-point was obtained after subtraction of the background following methodology described previously [23]. Integration was performed using a hybrid fit: a trapezoidal fit in the uptake phase and an exponential functional fit in the clearance phase. The total dose to the EL is the sum of the photon dose contribution from the brain and the remainder of the body, calculated using the brain as a surrogate target, and the total (photon plus electron) dose contribution from the LGs and tear film. The lens itself was not observed to concentrate activity, therefore no dose contribution from EL uptake was included in the AD calculation for the lens. In addition, we assumed that there was no uptake of activity in the eyeball, and that the activity in the LG is uniformly distributed and excreted exclusively via the tears.

The tear film dose contribution to the EL was determined by estimating the activity of the tear film using the measured time–activity data in the LG and a basal tear-production rate of 1.2 μl/min [31], and assuming that the activity clears from the LG via the tears at the same rate over the surface of the eye with a tear film thickness of 12 μm [32]. To calculate the TIA of the tear film, the time–activity data of the LG was fitted using the function given in Eq. 1:

$$A_{\mathrm{LG}}(t) = A_{\mathrm{LG}}(0) \cdot \mathrm{e}^{-\lambda t}(1 - \mathrm{e}^{-\kappa t}) \quad (1)$$

where $A_{\mathrm{LG}}(t)$ is the LG activity as a function of time and $A_{\mathrm{LG}}(0)$ is the activity at $t = 0$. Figure 3a shows the time–activity data for the LG in patient 1. The first derivative of the function given in Eq. 1, assuming a constant uptake function e^{-t}, yields the activity flow from the LG to the eye surface, assuming that the activity only clears from the LG via the tears following the baseline tear production rate and does not enter the bloodstream. Figure 3b shows the activity flow from the LG as a function of time in patient 1. The TIA of the tear film was also calculated using a second method based on the volume ratio between the LG (derived from VOIs drawn on CT images) and the tears. The volume of the tears was calculated using the surface area of the exposed open eye with a radius of 12 mm [26] and a tear film thickness of 12 μm [32]. This assumes that the activity concentration in the tears is the same as in the LG. The self-dose contribution of the LG is the product of the LG ← LG *S*-value and the LG TIA derived as described above. The total dose to the LG is the sum of the photon dose contribution from the brain and the remainder of the body, using the brain as a surrogate, plus the LG self-dose and the dose contribution from the contralateral LG to the LG.

Monte-Carlo based models were developed to estimate the AD to two major SG (the PG and SMG) using patient-specific anatomy. VOIs contouring the PG and SMG were drawn on the patients' CT images to determine the volumes of these glands. The drawn VOIs were converted to geometrical maps showing the specific patient's SG and were used as input in the Monte-Carlo simulation to generate patient-specific *S*-values for ^{18}F. The patient-specific 3D radiobiological dosimetry software (3D-RD) [33–36] using EGSnrc Monte Carlo was used for the simulation. The self-dose contribution of the PG/SMG is the product of the patient-specific *S*-values (PG←PG or SMG←SMG) and the TIACs for the PG and SMG, respectively. The cross-dose contribution from the SMG to the PG and vice-versa is the product of the patient-specific cross-dose *S*-value (PG←SMG and vice-versa) and the

TIAC of the source organ in each case. The total dose to the PG/SMG is the sum of the photon dose contribution to the PG/SMG from the brain and the remainder of the body, again using the brain as a surrogate target, and the self-dose contribution of the PG/SMG and the cross-dose contribution from the SMG/PG.

Results

The average age of the patients included in the study was 70 years, and their average weight and height were 82 kg and 175 cm [19]. Figure 4 shows maximum intensity projection PET images in one representative patient. The patient demonstrated physiological radiotracer uptake in the SG and LG, liver, spleen and small intestines. The activity from the blood pool cleared rapidly and significant renal excretion with radiotracer accumulation in the bladder was observed.

The TIACs for the organs of interest are listed in Table 1. The resultant mean AD per administered activity is given in Table 2 and Fig. 5. The LG received the highest AD of 0.242 mGy/MBq, followed by the SMG (0.093 mGy/MBq), kidneys (0.090 mGy/MBq), urinary bladder wall (0.087 mGy/MBq), PG (0.085 mGy/MBq) and liver (0.042 mGy/MBq).

The *S*-values from the eye model are listed in Table 3. The TIA values for the tear film are given in Table 4 for methods of calculation, activity flow and volume ratio between the LG and the tears. The difference between the values calculated using the activity flow from the LG and the volume ratio between the LG and the tears was 20 ± 33%.

The mean TIA of the LG and the tear film (activity flow/volume ratio methods) were 4.26E–04 min and 2.24E–07 min/2.77E–07 min, respectively. The dose contribution to the LG from the contralateral LG was calculated to be four orders of magnitude less than the LG self-dose. The dose to the EL includes dose contributions from both LGs (about 5% from the contralateral LG). The total AD to the EL averaged over nine patients was (1.3 ± 0.4) E–03 mGy/MBq. The average dose contributions from the LG and the tear film to the AD of the EL were 15% and 0.03%, respectively.

Table 5 lists the SG *S*-values for each patient, both self-doses and cross-doses, where the latter are from the PG to SMG and vice-versa. The mean *S*-values for the PG and SMG self-dose calculation were 3.58 and 6.78 mGy/MBq h, respectively. The mean cross-dose *S*-values were 0.0267 mGy/MBq h from the PG to SMG and 0.0264 mGy/MBq h from the SMG to PG. The resultant mean effective dose of ^{18}F-DCFPyL in the nine patients was 0.017 mSv/MBq (6.3 mSv, 0.63 rem) for an administered activity of 370 MBq (10 mCi).

Discussion

This dosimetry report presents AD results for the patient dataset of the first-in-human evaluation of the second-generation ^{18}F-labeled PSMA-targeted radiotracer ^{18}F-DCFPyL, and introduces Monte-Carlo-based models and previously unavailable organ *S*-values for the calculation of the doses to the nonstandard organs, including the EL and other small organs exhibiting uptake with this radio-tracer, that is the LG, PG and SMG. In our initial study, organ AD values were derived from four representative patients [19], and based on the initial

estimate of the organ AD to the EL, LG and SMG, the organs with the highest radiation dose were found to be the kidneys (0.095 mGy/MBq), followed by the urinary bladder wall (0.086 mGy/MBq), the SMG (0.039 mGy/MBq) and the liver (0.038 mGy/MBq) [19]. With the exception of the LG, PG and SMG, the average AD to the organs from nine patients is comparable to the previously reported dose values for these organs in four patients [19]. The AD to the EL, which accounts for the dose contribution from the LG and the tear film is comparable to the initial estimate which was equivalent to the photon AD received by the EL from the brain and the remainder of the body. These results for the EL show that the dose contribution from the tear film to the EL is negligible. This indicates that even if different values for the thickness as found in the literature [37] had been used this would not have affected the results. That the contribution from the tear film can be ignored is not surprising, but it is nevertheless important to have this validated.

The volume/size that was used in the initial estimation of the dose to the LG [19] was obtained by measuring the gland size from the patients' PET images. This over-estimation of the LG size resulted in a significant under-estimation of the AD to the LG. To correct for this, patient-specific VOIs were drawn on the CT images and were used to determine the "true" volume of the LG. The volumes derived from the VOIs drawn on the CT images were used in the Monte-Carlo model of the LG to determine the *S*-values needed for the dose calculations. The average ratio between the "PET size" and the "CT size" volume of the LG was 13 and is the main contributor to the ratio of 6.9 between the previously reported LG average AD and the current estimate.

The AD to the PG and SMG calculated using the Monte-Carlo model and the nine-patient dataset was 3.2 and 2.4 times higher than the previous calculations using the four-patient dataset of the AD to these glands, respectively. The ICRP 23 [26] determined volumes for PG and SMG, which were assumed in the initial dose estimates, were 1.1 and 1.5 times higher for the PG and SMG, respectively, than the CT-derived volumes which were used in the Monte-Carlo model. The model used patient-specific volumes and also accounted for the dose contribution from one SG to the other in addition to the glands' self-dose and the photon dose contribution from the brain to the glands, and therefore provides a more accurate estimate of the AD to the SG than the initial dose estimate which used reference human anatomic data for the SG and surrogate *S*-values.

The evaluation of ^{18}F-DCFPyL demonstrated favorable dosimetry with significantly lower doses to most radiosensitive organs compared with ^{18}F-DCFBC. The mean AD to the bone marrow for ^{18}F-DCFPyL was less than that for ^{18}F-DCFBC (17.0 ± 1.0 μGy/MBq). Similarly, the calculated mean effective dose for ^{18}F-DCFPyL is less than the mean effective dose for ^{18}F-DCFBC (19.9 ± 1.3 μSv/MBq).

A limitation of this study is the limited ability to correctly estimate the TIA using measurements obtained using an isotope with a relatively short half-life (^{18}F, half-life 109 min) and over a period of 120 min. This affected the smaller organs more than the larger ones, since some of the smaller organs were observed to still be in the biological uptake phase during the last measurement time-point in this study.

High activity uptake in the kidneys, bladder and SG has also been observed in previous studies evaluating the ^{68}Ga-PSMA targeted radioligands ^{68}Ga-PSMA-HBED-CC [38], ^{68}Ga-PSMA-I&T [39] and ^{68}Ga-PSMA-617 [40]. Organs with the highest AD of administered activity from the ^{68}Ga-labeled PSMA-targeted compounds are in general the urinary bladder wall, kidneys, spleen and liver. A comparison of the dosimetry results reported here and the dosimetry of ^{68}Ga-PSMA compounds shows that the ADs for ^{68}Ga compounds are generally higher than the ADs for ^{18}F-DCFPyL for these organs, with the exception of the liver for ^{68}Ga-PSMA-HBED-CC, the urinary bladder wall for ^{68}Ga-PSMA-I&T and the liver for ^{68}Ga-PSMA-617. Herrmann et al. [39] found that the AD values for the SG are lower than those for the spleen. Physiological uptake in the LG and the SG has been observed in recent radionuclide therapy studies using ^{177}Lu-PSMA-I&T [41] and ^{177}Lu-DKFZ-PSMA-617 [42]. The kidneys and the LG were found to be the organs receiving the highest AD, respectively, in these studies. However, the dosimetry calculations in these studies were based on information extracted from planar whole-body scintigraphy images, which are less accurate for measuring organ activities than 3D imaging modalities such as PET.

Conclusion

Dosimetry evaluation of^{18}F-DCFPyL in a nine-patient dataset and previously unavailable Monte-Carlo model-based dose estimates for the EL, LG and SMG for ^{18}F confirmed that PET imaging with ^{18}F-DCFPyL is feasible and safe. The organs that received the highest AD were the LG, SMG, kidneys, urinary bladder wall, and PG. These dose-limiting organs should be taken into account for the evaluation of this compound for possible use in the treatment of metastatic PCa. The Monte-Carlo models established in this study provided previously unavailable S-values for dose calculation to nonstandard organs including the EL, LG, and SG for ^{18}F. These models could be used in future studies to estimate the doses to these organs from other radioisotopes that may be of interest for both diagnostic and therapeutic purposes.

Acknowledgments

We acknowledge the support of the Prostate Cancer Foundation – Young Investigator Award, the Patrick C. Walsh Prostate Cancer Research Fund, EB006351, CA134675, CA184228, CA103175, CA183031 and CA116477.

References

1. Siegel RL, Miller KD, Jemal A. Cancer statistics, 2016. CA Cancer J Clin. 2016; 66:7–30. [PubMed: 26742998]
2. Ferlay J, Soerjomataram I, Dikshit R, et al. Cancer incidence and mortality worldwide: sources, methods and major patterns in GLOBOCAN 2012. Int J Cancer. 2015; 136:E359–86. [PubMed: 25220842]
3. Scher HI, Halabi S, Tannock I, et al. Design and end points of clinical trials for patients with progressive prostate cancer and castrate levels of testosterone: recommendations of the Prostate Cancer Clinical Trials Working Group. J Clin Oncol. 2008; 26:1148–59. [PubMed: 18309951]
4. Hofer C, Laubenbacher C, Block T, Breul J, Hartung R, Schwaiger M. Fluorine-18-fluorodeoxyglucose positron emission tomography is useless for the detection of local recurrence after radical prostatectomy. Eur Urol. 1999; 36:31–5.

5. Nuñez R, Macapinlac HA, Yeung HW, et al. Combined 18F-FDG and 11C-methionine PET scans in patients with newly progressive metastatic prostate cancer. J Nucl Med. 2002; 43:46–55. [PubMed: 11801702]
6. Shreve PD, Grossman HB, Gross MD, Wahl RL. Metastatic prostate cancer: initial findings of PET with 2-deoxy-2-[F-18]fluoro-D-glucose. Radiology. 1996; 199:751–6. [PubMed: 8638000]
7. Rowe SP, Gorin MA, Allaf ME, et al. PET imaging of prostate-specific membrane antigen in prostate cancer: current state of the art and future challenges. Prostate Cancer Prostatic Dis. 2016; 19:223–30. [PubMed: 27136743]
8. Hricak H, Choyke PL, Eberhardt SC, Leibel SA, Scardino PT. Imaging prostate cancer: a multidisciplinary perspective. Radiology. 2007; 243:28–53. [PubMed: 17392247]
9. Lawrentschuk N, Davis ID, Bolton DM, Scott AM. Positron emission tomography and molecular imaging of the prostate: an update. BJU Int. 2006; 97:923–31. [PubMed: 16643472]
10. De Jong I, Pruim J, Elsinga P, Vaalburg W, Mensink H. 11C-choline positron emission tomography for the evaluation after treatment of localized prostate cancer. Eur Urol. 2003; 44:32–9. [PubMed: 12814672]
11. Picchio M, Messa C, Landoni C, et al. Value of [11C] choline-positron emission tomography for re-staging prostate cancer: a comparison with [18F] fluorodeoxyglucose-positron emission tomography. J Urol. 2003; 169:1337–40. [PubMed: 12629355]
12. Greco C, Cascini G, Tamburrini O. Is there a role for positron emission tomography imaging in the early evaluation of prostate cancer relapse? Prostate Cancer Prostatic Dis. 2008; 11:121–8. [PubMed: 18180806]
13. Rahmim A, Zaidi H. PET versus SPECT: strengths, limitations and challenges. Nucl Med Commun. 2008; 29:193–207. [PubMed: 18349789]
14. Scattoni V, Picchio M, Suardi N, et al. Detection of lymph-node metastases with integrated [11 C] choline PET/CT in patients with PSA failure after radical retropubic prostatectomy: results confirmed by open pelvic-retroperitoneal lymphadenectomy. Eur Urol. 2007; 52:423–9. [PubMed: 17397992]
15. Schuster DM, Nanni C, Fanti S. PET tracers beyond FDG in prostate cancer. Semin Nucl Med. 2016; 46:507–21. [PubMed: 27825431]
16. Pandit-Taskar N, O'Donoghue JA, Durack JC, et al. A phase I/II study for analytic validation of 89Zr-J591 immunoPET as a molecular imaging agent for metastatic prostate cancer. Clin Cancer Res. 2015; 21:5277–85. [PubMed: 26175541]
17. Chen Y, Pullambhatla M, Foss CA, et al. 2-(3-{1-Carboxy-5-[(6-[18F]fluoro-pyridine-3-carbonyl)-amino]-pentyl}-ureido)-pentanedioic acid, [18F]DCFPyL, a PSMA-based PET imaging agent for prostate cancer. Clin Cancer Res. 2011; 17:7645–53. [PubMed: 22042970]
18. Cho SY, Gage KL, Mease RC, et al. Biodistribution, tumor detection, and radiation dosimetry of 18F-DCFBC, a low-molecular-weight inhibitor of prostate-specific membrane antigen, in patients with metastatic prostate cancer. J Nucl Med. 2012; 53:1883–91. [PubMed: 23203246]
19. Szabo Z, Mena E, Rowe SP, et al. Initial evaluation of [(18)F]DCFPyL for prostate-specific membrane antigen (PSMA)-targeted PET imaging of prostate cancer. Mol Imaging Biol. 2015; 17:565–74. [PubMed: 25896814]
20. Evangelista L, Briganti A, Fanti S, et al. New clinical indications for 18F/11C-choline, new tracers for positron emission tomography and a promising hybrid device for prostate cancer staging: a systematic review of the literature. Eur Urol. 2016; 70:161–75. [PubMed: 26850970]
21. Stabin MG, Sparks RB, Crowe E. OLINDA/EXM: the second-generation personal computer software for internal dose assessment in nuclear medicine. J Nucl Med. 2005; 46:1023–7. [PubMed: 15937315]
22. Bolch WE, Eckerman KF, Sgouros G, Thomas SR. MIRD pamphlet no. 21: a generalized schema for radiopharmaceutical dosimetry – standardization of nomenclature. J Nucl Med. 2009; 50:477–84. [PubMed: 19258258]
23. Plyku D, Hobbs RF, Huang K, et al. Recombinant human thyroid-stimulating hormone versus thyroid hormone withdrawal in 124I-PET/CT based dosimetry for 131I therapy of metastatic differentiated thyroid cancer. J Nucl Med. 2017; 58:1146–54. [PubMed: 28104741]

24. ICRP. Basic anatomical and physiological data for use in radiological protection: reference values. A report of age- and gender-related differences in the anatomical and physiological characteristics of reference individuals. ICRP Publication 89. Ann ICRP. 2002; 32:5–265. [PubMed: 14506981]
25. SAAM II User Guide. Seattle: SAAM Institute, University of Washington; 1997.
26. Snyder, WS., Cook, MJ., Nasset, ES., Karhausen, LR., Howells, GP., Tipton, IH. ICRP publication 23. Elmsford, NY: International Commission on Radiological Protection; 1975. Report of the task group on reference man.
27. ICRP. 1990 Recommendations of the International Commission on Radiological Protection. ICRP publication 60. Ann ICRP. 1991; 21(1–3)
28. Thomas SR, Stabin MG, Chen CT, Samaratunga RC. MIRD Pamphlet No. 14: a dynamic urinary bladder model for radiation dose calculations. J Nucl Med. 2012; 33:783–802.
29. Agostinelli S, Allison J, Amako KA, et al. GEANT4 – a simulation toolkit. Nucl Instrum Methods Phys Res A. 2003; 506:250–303.
30. Tamboli DA, Harris MA, Hogg JP, Realini T, Sivak-Callcott JA. Computed tomography dimensions of the lacrimal gland in normal Caucasian orbits. Ophthalmic Plast Reconstr Surg. 2011; 27:453–6.
31. Price KM, Richard MJ. Ophthalmic Pearls: The tearing patient: diagnosis and management. EyeNet Magazine. 2009:33–5.
32. Montés-Micó R. Role of the tear film in the optical quality of the human eye. J Cataract Refract Surg. 2007; 33:1631–5. [PubMed: 17720082]
33. Sgouros G, Frey E, Wahl R, He B, Prideaux A, Hobbs R. Three-dimensional imaging-based radiobiological dosimetry. Semin Nucl Med. 2008; 38:321–34. [PubMed: 18662554]
34. Prideaux AR, Song H, Hobbs RF, et al. Three-dimensional radio-biologic dosimetry: application of radiobiologic modeling to patient-specific 3-dimensional imaging-based internal dosimetry. J Nucl Med. 2007; 48:1008–16. [PubMed: 17504874]
35. Sgouros G, Hobbs RF, Atkins FB, Van Nostrand D, Ladenson PW, Wahl RL. Three-dimensional radiobiological dosimetry (3D-RD) with 124I PET for 131I therapy of thyroid cancer. Eur J Nucl Med Mol Imaging. 2011; 38(Suppl 1):S41–7. [PubMed: 21484384]
36. Hobbs RF, Wahl RL, Lodge MA, et al. 124I PET-Based 3D-RD dosimetry for a pediatric thyroid cancer patient: real time treatment planning and methodologic comparison. J Nucl Med. 2009; 50(11):1844–47. [PubMed: 19837771]
37. King-Smith PE, Fink BA, Hill RM, Koelling KW, Tiffany JM. The thickness of the tear film. Curr Eye Res. 2004; 29:357–68. [PubMed: 15590483]
38. Pfob CH, Ziegler S, Graner FP, et al. Biodistribution and radiation dosimetry of 68Ga-PSMA HBED CC – a PSMA specific probe for PET imaging of prostate cancer. Eur J Nucl Med Mol Imaging. 2016; 43:1962–70. [PubMed: 27207281]
39. Herrmann K, Bluemel C, Weineisen M, et al. Biodistribution and radiation dosimetry for a probe targeting prostate-specific membrane antigen for imaging and therapy. J Nucl Med. 2015; 56:855–61. [PubMed: 25883128]
40. Afshar-Oromieh A, Hetzheim H, Kratochwil C, et al. The theranostic PSMA ligand PSMA-617 in the diagnosis of prostate cancer by PET/CT: biodistribution in humans, radiation dosimetry, and first evaluation of tumor lesions. J Nucl Med. 2015; 56:1697–705. [PubMed: 26294298]
41. Okamoto S, Thieme A, Allmann J, et al. Radiation dosimetry for 177Lu-PSMA I&T in metastatic castration-resistant prostate cancer: absorbed dose in normal organs and tumor lesions. J Nucl Med. 2017; 58:445–50. [PubMed: 27660138]
42. Hohberg M, Eschner W, Schmidt M, et al. Lacrimal glands may represent organs at risk for radionuclide therapy of prostate cancer with [(177)Lu]DKFZ-PSMA-617. Mol Imaging Biol. 2016; 18:437–45. [PubMed: 26920354]

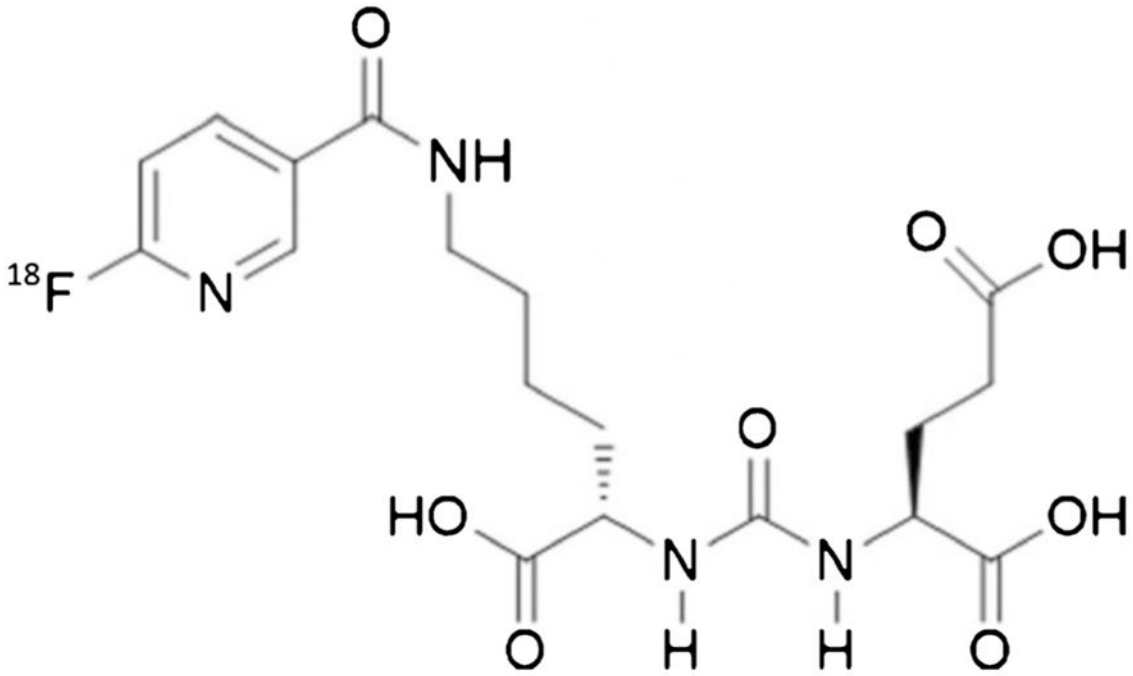

Fig. 1.
Chemical structure of ^{18}F-DCFPyL

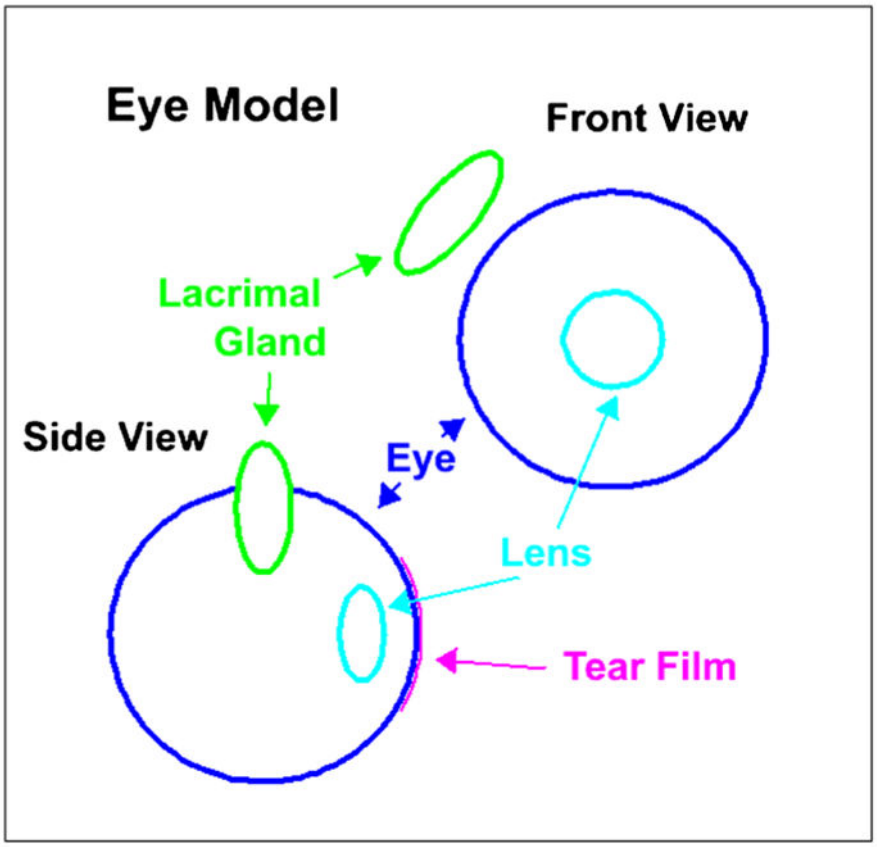

Fig. 2.
Model representation of the eyeball, eye lens and lacrimal gland

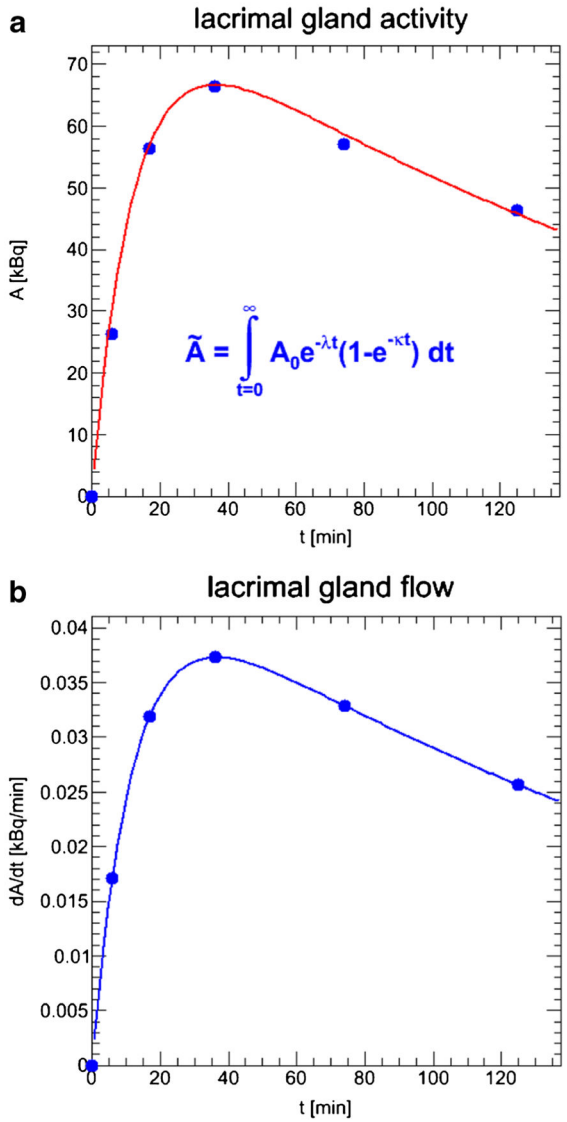

Fig. 3.

Estimation of the activity flow from the lacrimal gland to the eye surface via the tears: **a** time–activity data for the lacrimal glands; **b** activity flow from the lacrimal gland via the tears

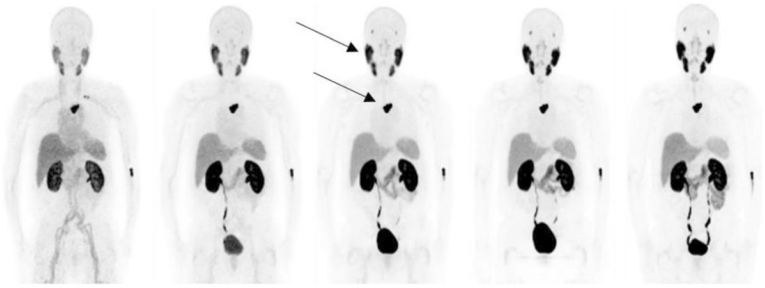

Fig. 4.

Maximum intensity projection PET images in a representative patient. The images show physiological tracer uptake in the salivary glands (upper arrow), lacrimal glands, kidneys, liver, spleen, small intestine and urinary excretion. Uptake is also seen in a metastatic lesion in the spine (lower arrow).

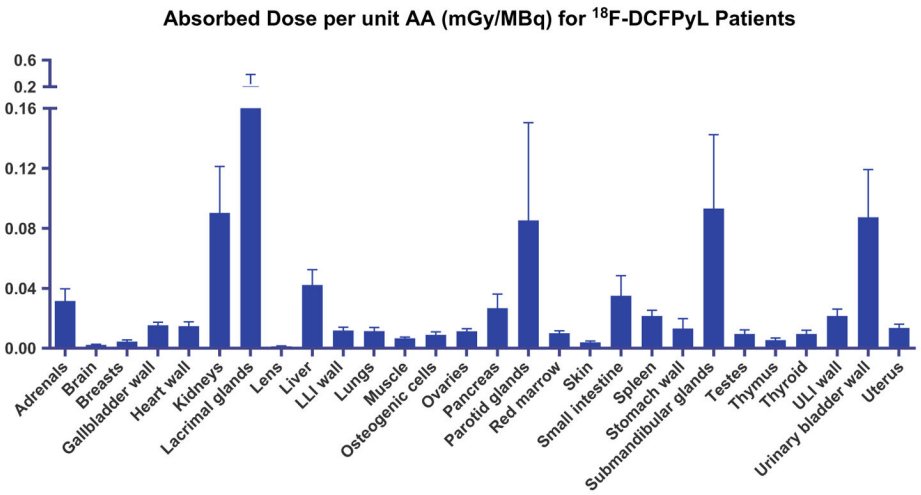

Fig. 5.

Absorbed dose per unit administered activity of selected organs for ^{18}F-DCFPyL in nine patients (*LLI* lower large intestine, *ULI* upper large intestine)

Table 1

Time-integrated activity coefficients (TIAC) of selected organs for ^{18}F-DCFPyL in nine patients

Organ	Mean TIAC [(Bq h)/Bq]	Standard deviation [%]
Adrenals	2.91E–04	0.01
Bone marrow (spine)	4.68E–02	2.35
Brain	5.37E–03	0.10
Gallbladder	1.13E–03	0.05
Heart	2.31E–02	0.62
Heart wall	7.99E–03	0.31
Kidneys	1.89E–01	8.44
Lacrimal glands	4.26E–04	0.02
Lens	3.41E–06	0.00
Liver	2.56E–01	8.07
Lower large intestine	3.71E–03	0.19
Lungs	4.15E–02	1.27
Muscle	3.23E–01	7.53
Pancreas	2.63E–03	0.13
Parotid glands	2.16E–02	1.16
Spleen	1.74E–02	1.19
Stomach	1.42E–02	1.79
Submandibular glands	9.55E–03	0.42
Testes	1.22E–03	0.08
Thyroid	2.56E–04	0.01
Upper large intestine	2.42E–02	1.10
Urinary bladder contents	1.73E–01	6.78
Small intestine	1.35E–01	7.34
Total body	1.92E00	28.63
Remainder of body	6.16E–01	30.94

Table 2

Absorbed doses per unit administered activity of selected organs for ^{18}F-DCFPyL in nine patients

Organ	Absorbed dose [mGy/MBq]	Standard deviation [%]
Adrenals	3.15E–02	0.81
Brain	2.15E–03	0.05
Breasts	4.36E–03	0.12
Gallbladder wall	1.53E–02	0.21
Heart wall	1.46E–02	0.31
Kidneys	9.03E–02	3.11
Lacrimal glands	2.42E–01	14.18
Lens	1.19E–03	0.04
Liver	4.22E–02	1.02
Lower large intestine wall	1.18E–02	0.21
Lungs	1.15E–02	0.24
Muscle	6.57E–03	0.09
Osteogenic cells	8.95E–03	0.20
Ovaries	1.13E–02	0.17
Pancreas	2.67E–02	0.94
Parotid glands	8.52E–02	6.52
Red marrow	9.98E–03	0.17
Skin	3.91E–03	0.10
Small intestine	3.50E–02	1.34
Spleen	2.15E–02	0.38
Stomach wall	1.31E–02	0.68
Submandibular glands	9.33E–02	4.92
Testes	9.58E–03	0.26
Thymus	5.41E–03	0.14
Thyroid	9.49E–03	0.26
Upper large intestine wall	2.15E–02	0.47
Urinary bladder wall	8.73E–02	3.20
Uterus	1.36E–02	0.24

Table 3

Patient-specific *S*-values for the eye lens (EL) and the lacrimal gland (LG) for dose calculation

Patient	Mass of LG [g]	*S*-value [mGy/MBq h]	
		EL ← LG	LG ← LG
1	0.213	0.416	532.3
2	0.184	0.403	611.1
3	0.262	0.427	437.6
4	0.166	0.407	673.1
5	0.277	0.429	415.1
6	0.175	0.429	432.5
7	0.200	0.414	567.7
8	0.157	0.415	713.4
9	0.142	0.410	784.1

Table 4

Time-integrated activity coefficients (TIAC) for lacrimal glands (LG) and tears

Patient	TIAC [min]		
	LG	Tear film	
		Based on activity flow	Based on volume ratio
1	8.45E–04	4.73E–07	5.36E–07
2	5.15E–04	2.30E–07	3.77E–07
3	2.70E–04	1.92E–07	1.39E–07
4	4.12E–04	2.30E–07	3.34E–07
5	2.80E–04	1.08E–07	1.37E–07
6	5.56E–04	4.36E–07	4.29E–07
7	2.61E–04	1.02E–07	1.77E–07
8	6.17E–04	1.38E–07	3.28E–07
9	0.8E–04	1.03E–07	3.93E–08

Table 5

Patient-specific *S*-values for the parotid glands (PG) and submandibular glands (SMG) for dose calculation

Patient	Mass of PG [g]	*S*-value [mGy/MBq h]		Mass of SMG [g]	*S*-value (mGy/MBq h)	
		PG ←PG	PG ←SMG		SMG ←SMG	SMG ←PG
1	36.4	4.2E00	2.3E–02	16.7	8.8E00	2.3E–02
2	45.9	3.4E00	2.4E–02	9.2	1.6E01	2.4E–02
3	56.5	2.8E00	2.3E–02	30.4	5.0E00	2.3E–02
4	45.1	3.4E00	3.7E–02	14.6	9.9E00	3.7E–02
5	53.5	2.9E00	2.4E–02	15.2	9.6E00	2.4E–02
6	43.8	3.5E00	3.0E–02	18.0	8.2E00	3.0E–02
7	49.0	3.2E00	2.2E–02	12.5	1.2E01	2.3E–02
8	30.4	4.9E00	2.5E–02	14.8	1.0E01	2.5E–02
9	37.4	4.0E00	3.1E–02	22.1	6.8E00	3.1E–02